Geophysical Journal International

Geophys. J. Int. (2010) **181,** 1109–1127 doi: 10.1111/j.1365-246X.2010.04561.x

Cross-correlation weighted migration: towards high-resolution mapping of mantle heterogeneities

Tadashi Kito and Jun Korenaga

Department of Geology and Geophysics, Yale University, New Haven, CT, USA. E-mail: jun.korenaga@yale.edu

Accepted 2010 February 10. Received 2010 February 10; in original form 2009 July 31

SUMMARY

We present a new type of Born migration scheme to obtain a high-resolution image of small-scale scatterers in the mantle. Seismic migration is a technique that projects scattered energy back to its origin by shifting and stacking seismograms using theoretical traveltimes. Migration methods in global seismology, because of the limited distribution of sources and receivers, tend to suffer from considerable smearing owing to isochronal artefacts. This type of artefacts is caused by migration grids that have the set of theoretical traveltimes (from a given source to all receivers) similar to that for a true scattering point. Previously, the information of slowness and backazimuth was explicitly explored to reduce such migration artefacts. Here we propose a simpler and more computationally efficient method but with similar effects, in which the coherency of shifted seismograms measured by cross-correlation is exploited to suppress isochronal artefacts. The new migration scheme makes it possible to compute a large number of migrated images efficiently and thus evaluate the robustness of observed scattering objects by statistical approaches such as bootstrap resampling.

Key words: Mantle processes; Body waves; Wave scattering and diffraction.

1 MOTIVATION

The presence of chemical heterogeneities in Earth's mantle has long been suggested by geochemical studies (e.g. Allègre & Turcotte 1986; Zindler & Hart 1986; Hofmann 1997; Korenaga & Kelemen 2000), though the spatial distribution of such heterogeneities is poorly constrained. They may exist as a large-scale reservoir in the deep mantle (e.g. Kellogg *et al.* 1999) or may be dispersed in the entire mantle as numerous blobs of various scales (e.g. Helffrich & Wood 2001; Ito & Mahoney 2005; Lyubetskaya & Korenaga 2007). One important fact is that chemical heterogeneities are continuously produced by plate tectonics. Magmatism beneath mid-ocean ridges differentiates source mantle into oceanic crust and depleted mantle lithosphere, both of which are eventually transported back into the deep mantle by subduction. The fate of these subducted materials is essential to understand the structure and evolution of Earth's mantle (e.g. Christensen & Hofmann 1994; van Keken *et al.* 2002; Korenaga 2008a,b), but it remains largely unresolved. Mantle convection may not efficiently mix the oceanic crust and the depleted mantle (Manga 1996), and the vigor of convection itself may have been weaker in the past (Korenaga 2006). Also, mantle convection does not necessarily homogenize chemically differentiated components; subducted crust and lithospheric mantle could follow different trajectories (e.g. Ringwood & Irifune 1988; van Keken *et al.* 1996; Karato 1997; Lee & Chen 2007), and there may be regions locally enriched (or depleted) with recycled oceanic crust. As a source mantle enriched in the crustal component is more fertile (i.e. prone to melt), such chemical heterogeneities have an important bearing on the origin of hotspots and large igneous provinces (e.g. Sleep 1984; Cordery *et al.* 1997; Korenaga 2004, 2005). Plate tectonics may thus naturally produce a chemically heterogeneous mantle at various scales, with profound implications for terrestrial magmatism and mantle convection, but geophysical constraints on the actual extent of chemical heterogeneities have been rather limited.

In the last decade or so, seismic tomography has revealed the complex behaviour of subducted slabs; some slabs seem to penetrate deeply into the lower mantle (e.g. van der Hilst *et al.* 1997; Karason & van der Hilst 2001) whereas others may be stagnant in the transition zone (e.g. Fukao *et al.* 2001). Because small-scale features tend to be smoothed out by regularization, however, a tomographic approach is not suited to resolve chemical heterogeneities except at very large scales (e.g. Kennett *et al.* 1998; Trampert *et al.* 2004). The existence of small-scale heterogeneities, therefore, has been hinted by other types of seismological studies. The amplitude of PKP precursors, for example, suggests the global occurrence of small-scale ($< \sim$8 km) heterogeneities throughout the mantle (e.g. Hedlin *et al.* 1997; Margerin & Nolet 2003). More direct evidence for individual heterogeneities can be obtained by seismic array methods, and both *S*-to-*P* conversions and *P*-to-*P* reflections have been identified from some subducted slabs in the mid- and lower mantle (e.g. Kaneshima & Helffrich 1999; Kaneshima 2003; Vanacore *et al.* 2006; Kito *et al.* 2008; Rost *et al.* 2008). These studies tend to interpret the observed scattering objects as spatially

coherent features such as dipping reflectors. The resolution of teleseismic migration is still to be improved in order to confidently characterize smaller-scale heterogeneities unbiased by their topology, but such information is what is critically needed to delineate the present state of the chemically heterogeneous mantle.

Identifying discontinuous structures such as blobs is, however, challenging. Imaging by seismic array methods tends to suffer from various artefacts, and it is usually difficult to interpret small-scale features with confidence. Consider, for example, seeing a few isolated scatterers in an image produced by seismic migration. If they are characterized by weak amplitudes and are not correlated well with tomographic images, it may be tempting to disregard their significance, though they might correspond to crustal fragments segregated from a sinking slab. To interpret such subtle features, we need to first establish their robustness, and to this end, we need a seismic array method that not only can suppress artefacts but also is computationally efficient. Demonstrating the statistical reliability of a certain signal in a robust manner usually requires computationally intensive schemes such as bootstrap resampling, so developing a rapid method with artefact suppression is an essential step to achieve the high-resolution imaging of chemical heterogeneities in the mantle. The purpose of this paper is to report a new seismic migration scheme developed along this line of effort. We will begin with the overview of existing migration methods, followed by the description of our migration procedure. The results of synthetic tests will then be given, and the new method is also compared with previous methods using real data. We will discuss the possibility of different implementation as well as the issue of numerical efficiency at the end.

2 THE BACKGROUND OF SEISMIC MIGRATION

Seismic migration is a data-processing technique that projects seismic energy observed at receivers back to its origin, thereby reconstructing the image of Earth's interior. A background velocity structure must be known *a priori* for this back projection. Seismic migration was originally developed in exploration geophysics to locate subsurface heterogeneities related to natural resources such as oil and gas. As high-quality teleseismic data have been accumulated, migration has become popular in global seismology to image scatterers and reflectors in the crust and the mantle (e.g. Revenaugh 1995; Freybourger *et al.* 2001; Thomas *et al.* 2004; Chambers & Woodhouse 2006; Hutko *et al.* 2006, 2008).

Any migration method intrinsically involves the calculation of isochronal surfaces. For a given source–receiver pair, one can always define isochronal surfaces; scatterers located on the same isochronal surface share the same theoretical traveltime for scattered waves. (Fig. 1), so the origin of scattered energy cannot be located using one receiver. The use of a seismic array can alleviate this non-uniqueness problem. A number of receivers can be used to identify the intersection of all of relevant isochronal surfaces, thereby better localizing the true origin of scattering energy. In global seismology, however, the aperture of an array is usually not sufficiently large, and ray paths are often restricted to one direction owing to limited source and receiver locations. If the distribution of isochronal surfaces is biased towards a particular direction, the scattered energy can still be stacked constructively around such direction, appearing as artefacts along the isochronal surfaces. We refer to such collection of migration grids with similar sets of source–receiver traveltimes as a 'quasi-isochronal volume', and different scatterer locations are associated with different volumes (Fig. 2). Achieving an artefact-free high-resolution image of scatterers is difficult, especially in the deep mantle, because the size of this volume is often non-trivial.

Various migration techniques were developed to reduce isochronal artefacts and improve the resolution of a migrated image. Lay & Young (1996) and Bilek & Lay (1998), for example, used relative traveltimes between a reference phase and scattered waves to narrow down the possible regions of scatterers. Krüger *et al.* (1996) proposed to use source and receiver arrays simultaneously, and based on this double-beam scheme, Scherbam *et al.* (1997) calculated the probability distributions of traveltime, slowness, and azimuth to estimate the likelihood of scatterings in the lowermost mantle. Although implementation may appear to be quite different, common philosophy behind these studies is to minimize the location of potential scattering points by exploiting subtle traveltime differences of observed scattered waves arriving at different stations.

Migration methods explicitly using such information for deblurring have also been developed. To investigate the structure of the D'' layer, Kito & Krüger (2001) integrated the phase-weighted stacking technique of Schimmel & Paulssen (1997), which is an amplitude-independent measure of coherency, into a conventional migration scheme. Most recently, Kito *et al.* (2007) developed a high-resolution migration method by calculating an appropriate data weighting based on the slowness and backazimuth of observed scattered waves. This method is, however, not computationally efficient because a large number of stacking processes are needed to explore the slowness and backazimuth field. Subtle traveltime differences within a quasi-isochronal volume, however, can be exploited more directly using cross-correlation, without being translated into backazimuth and slowness. This notion is the foundation of our migration scheme as described in the next section.

3 METHOD

3.1 Basic migration process

To set up notations, let us consider a target volume defined in a certain region of interest with a constant grid interval. Each gridpoint serves as a potential isotropic single scatterer. Using a reference earth model, theoretical traveltimes are calculated for potential scattered waves that propagate from a source via gridpoints, $G_i (i = 1, 2, \ldots, N_g)$, to all seismic stations, $R_j (j = 1, 2, \ldots, N_r)$. For each gridpoint G_i, relative traveltimes between a reference seismic phase and relevant scattered waves are used to shift seismograms, and the shifted seismograms are stacked within a certain time window. The midpoint of the time window corresponds to the theoretical traveltime of a potential scattered wave at each receiver.

The maximum energy of stacked waveforms is then defined as migrated energy, that is,

$$E_i = \max \left[\frac{1}{N_r} \left(\sum_{j=1}^{N_r} W(\Delta t_{\mathrm{w}}) S_j \left(t - t_{ij}^0 + t_j^r \right) \right)^2 \right], \tag{1}$$

where

$$W(\Delta t_{\mathrm{w}}) = \begin{cases} 1 & \text{if } |t| < \Delta t_{\mathrm{w}}/2 \\ 0 & \text{otherwise.} \end{cases} \tag{2}$$

Here E_i is migrated energy for the gridpoint G_i, S_j is the seismogram recorded at the jth station R_j as a function of time t, t_{ij}^0 is the theoretical traveltime of a scattered wave arriving at R_j through G_i, t_j^r is the

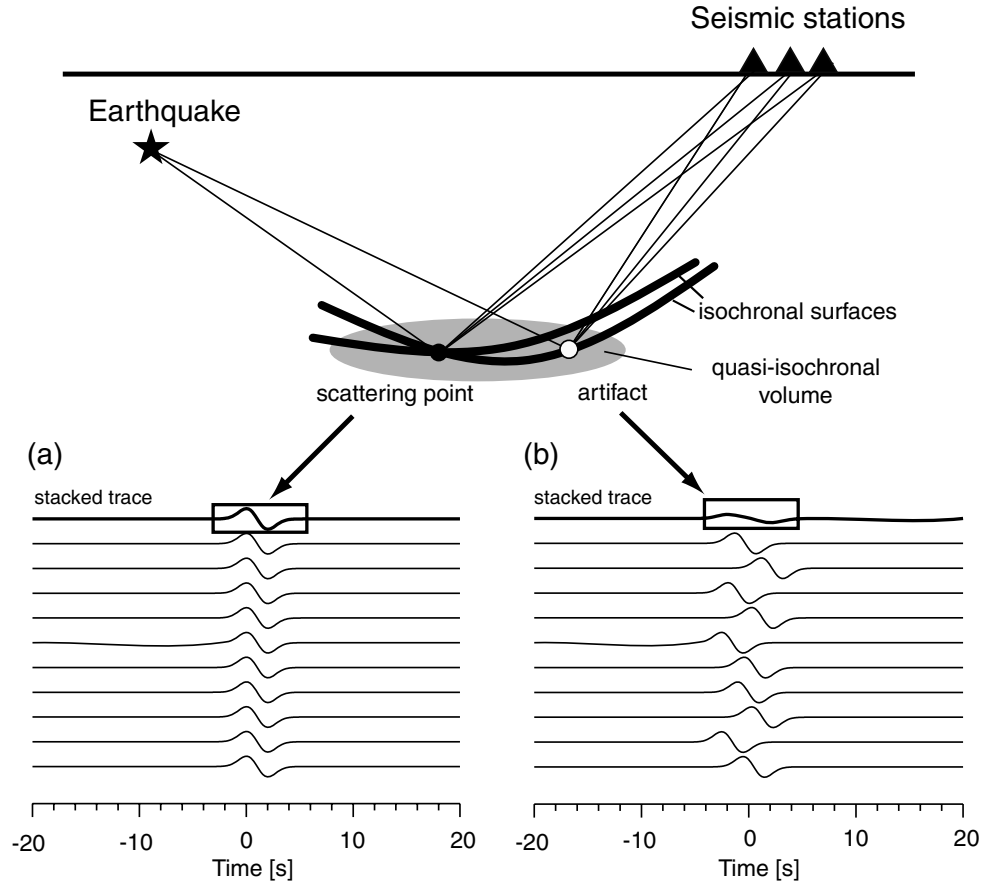

Figure 1. Schematic diagram to illustrate the variation of waveform coherency along an isochronal surface (thick line), any scattering at which has the same traveltime with respect to a given source–receiver combination. Solid circle on the isochronal surface denotes a true scattering point, and open circle exemplifies isochronal artefact. (a) Seismograms are shifted with respect to the scattering point (solid circle). At the true scattering point, traces are expected to align perfectly so that stacked energy takes the maximum. (b) Seismograms are shifted with respect to another point along the isochronal surface (open circle). Even off the true scattering point, various isochrons still graze and overlap each other, constituting a quasi-isochronal volume (shown by grey shading) and resulting in an incomplete cancellation of seismic energy. Top waveforms (thick lines) in both panels are stacked seismograms using all traces. Boxes denote a typical time window used to define scattered energy.

theoretical traveltime of the reference phase at R_j, and $W(\Delta t_w)$ is the window function. The length of the time window, Δt_w, may be set to the dominant frequency of observed waveforms. As mentioned in the introduction section, this simple procedure is known to yield a migration image usually contaminated by isochronal artefacts.

3.2 Cross-correlation weighting

Any quasi-isochronal volume contains a single true scattering point, at which scattered waves are expected to have a perfect alignment after shifting seismograms with respect to the scattering point (Fig. 1). As moving away from this point, the alignment of shifted traces deteriorates, gradually along the dominant trend of the quasi-isochronal volume and more rapidly in other directions. In the framework of the slowness and backazimuth weighted migration of Kito *et al.* (2007), such deterioration is quantified as the difference between the theoretical and observed values of slowness and backazimuth, and this difference is used to weight stacked energy. Calculating observed slowness and backazimuth is, however, a time-consuming process, which has to be repeated for each gridpoint.

Alternatively, we can measure the quality of trace alignment more directly by cross-correlation, thereby calculating a weighting factor more rapidly. After shifting seismograms with respect to a given gridpoint as described in the previous section, we calculate the cross-correlation coefficient of a reference seismogram and each of other seismograms. Here we arbitrarily choose the first station's data, S_1, as a reference. When incorporating a statistical approach such as bootstrap resampling, this reference station may be selected differently for each bootstrap ensemble to minimize any bias introduced by this arbitrary selection. At the gridpoint G_i, the cross-correlation coefficient for other stations $R_j (j = 2, 3, \ldots, N_r)$ may be defined as

$$C_{ij}(\delta t) = \frac{\int [S_j(\tau + \delta t) - \overline{S_j(\tau + \delta t)}][S_1(\tau) - \overline{S_1(\tau)}]\mathrm{d}\tau}{\left\{\int [S_j(\tau + \delta t) - \overline{S_j(\tau + \delta t)}]^2 \mathrm{d}\tau\right\}^{1/2} \left\{\int [S_1(\tau) - \overline{S_1(\tau)}]^2 \mathrm{d}\tau\right\}^{1/2}}, \quad (3)$$

where τ represents $(t - t_{ij}^0 + t_j^r)$ in eq. (1), the range of integration is from $-\Delta t_w/2$ to $\Delta t_w/2$, and bars indicate averaging. The coefficient is a function of time-shift δt and can take a value from -1 to 1. Two waveforms are generally considered to be coherent when their cross-correlation is close to 1, so when the coefficient has a maximum

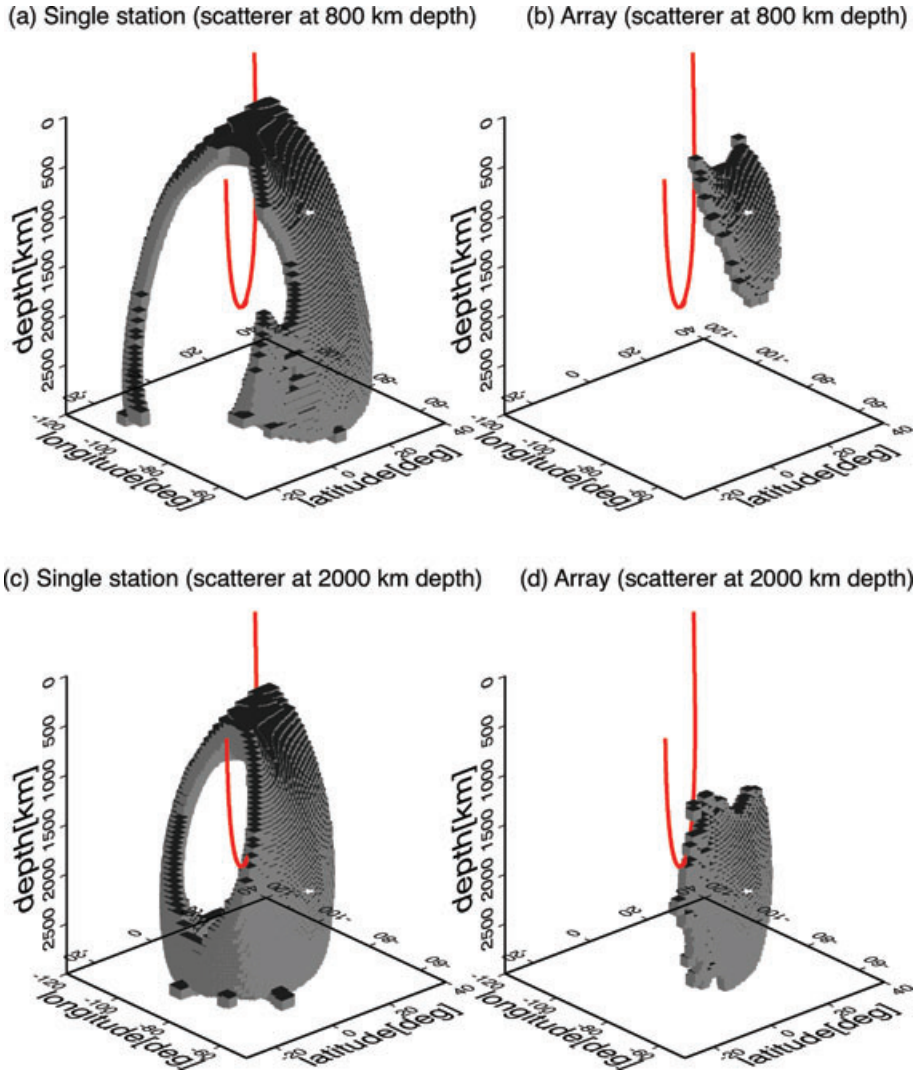

Figure 2. Distribution of gridpoints contained in a quasi-isochronal volume, whose (average) theoretical traveltimes are virtually identical to that of the true scattering point (shown by star). Red curve indicates the ray path of direct *P* wave. These examples are all based on the source–receiver geometry shown in Fig. 3. (a) The scatterer is located at the depth of 800 km. Only one station is used to define isochronal grids. (b) Same as (a) but with all 24 stations. (c) Same as (a) but at the depth of 2000 km. (d) Same as (c) but with all stations.

during the systematic shift of S_j, we take the corresponding time-shift as the time offset for the station R_j at the gridpoint G_i and denote it as δt_{ij}. After estimating time offsets for all but reference stations, the variance of time offsets is calculated as

$$\sigma_i^2 = \frac{1}{N_r - 1} \sum_{j=2}^{N_r} \delta t_{ij}^2. \tag{4}$$

Using this variance as a measure of proximity to a true scattering point, we propose the following weighting scheme

$$E_i^* = E_i \exp\left[-\frac{\sigma_i^2}{(\alpha \Delta t_w)^2} \right], \tag{5}$$

where α is a constant and E_i^* is weighted migrated energy. A small variance indicates a nearly perfect alignment of waveforms, in which case almost no weighting is applied to migrated energy. Conversely, a large variance suggests that the corresponding migrated energy is likely to be an isochronal artefact. The constant α controls the strength of weighting, and an optimal value of α needs to be determined empirically, for example, by synthetic tests. Smaller α leads to stronger weighting, but too small α starts to reduce even correct signals because various factors such as the presence of noise and an incorrect background velocity model can disturb otherwise perfect cross-correlation. We may thus need to be conservative when choosing a value for α by taking data quality into account. The normalization of variance by $(\alpha \Delta t_w)^2$ in the above formulation is to make our weighting scheme less frequency-dependent.

3.3 Combining semblance with cross-correlation

When applying cross-correlation weighting to real data, the presence of noise may degrade the accuracy of time-offset measurements if the noise level is sufficiently large. To make the new weighting method more stable with respect to noise, we combined cross-correlation with semblance (Neidell & Taner 1971), which is a coherency measure that is insensitive to the amplitude of coherent signals. The semblance coefficient at the gridpoint G_i may be

defined as

$$Sc_i = \frac{\int \left[\sum_{j=1}^{N_r} S_j(\tau) \right]^2 \mathrm{d}\tau}{N_r \sum_{j=1}^{N_r} \left[\int S_j(\tau)^2 \mathrm{d}\tau \right]}, \quad (6)$$

where the range of integration and the definition of τ are the same as for eq. (3). The semblance coefficient ranges from 0 to 1. In contrast to cross-correlation, semblance is a multichannel coherence measure and relatively robust in noisy data. When the alignment of coherent signals is optimal, the semblance coefficient is expected to be high. To combine cross-correlation and semblance, we use the following linear mixing

$$W = W_{\mathrm{cc}}\overline{C} + W_{\mathrm{sem}}(1 - \overline{C}), \quad (7)$$

where W_{cc} is the weighting factor determined by cross-correlation, W_{sem} is the weighting factor determined by semblance, and $\overline{C}$ is the average of the maximum cross-correlation coefficients that are used to determine the time offsets δt_j. Lower $\overline{C}$ corresponds to less successful calculation of cross-correlation, and the overall weighting relies more on semblance using the above mixing formula. Since cross-correlation is more direct measure of waveform coherency, weighting with cross-correlation is more effective for the suppression of isochronal artefacts than that with semblance. Therefore, it is desirable that cross-correlation is used for weighting as long as it is functional, and semblance is used to compensate for cross-correlation only when $\overline{C}$ is small due to noisy data. Using the eqs (5)–(7), the weighted migrated energy at the gridpoint G_i may be rewritten as

$$E_i^* = E_i \left\{ \overline{C}_i \exp\left[-\frac{\sigma_i^2}{(\alpha \Delta t_{\mathrm{w}})^2} \right] + (1 - \overline{C}_i) Sc_i \right\}, \quad (8)$$

which takes advantage of the two measures, cross-correlation and semblance, by automatically changing their contributions based on the signal-to-noise ratio of real data. Since semblance is also affected by noise, its coefficient is usually not unity in the presence of noise even if coherent waveforms are perfectly aligned. The semblance coefficient may be normalized by the maximum (among all gridpoints) so that the amplitude of coherent waveforms is not adversely affected by weighting with semblance.

4 BENCHMARK TESTS

4.1 Synthetics and data

We performed several benchmark tests to validate our approach using both synthetic and real data. We set up a 3-D volume with a grid interval of 50 km in the whole mantle (from Earth's surface to the core–mantle boundary) beneath Central America (Fig. 3). The lateral extension of the grid volume is 4000 km both in the E–W and N–S directions. For a source, we used an intermediate-depth event in South America (latitude $= -19.78^\circ$, longitude $= -68.98^\circ$, and depth $= 113$ km with the origin time of 02:39:40.37 on 2005 August 14). The source parameters were taken from the NEIC PDE catalogue, and the source mechanism was taken from the Harvard CMT catalogue. For receivers, we used the TriNET seismic network, which is composed of 24 stations in California. A low-pass filter with the corner frequency of 0.5 Hz was applied to broadband seismic data from this receiver array (Fig. 4). The duration of the

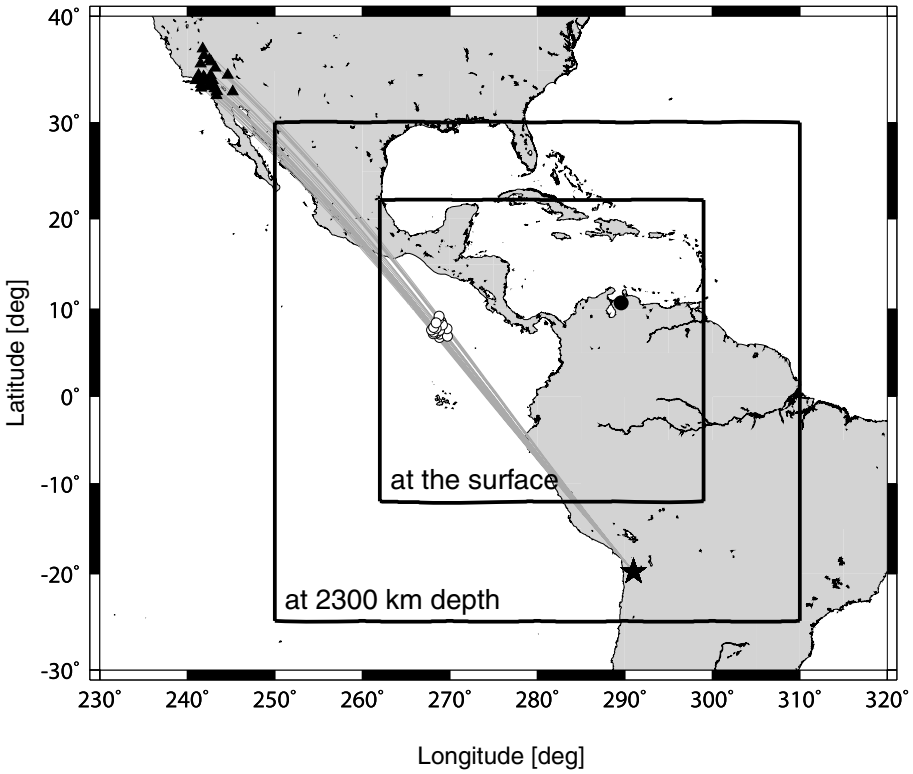

Figure 3. Locations of the event (star) and stations (solid triangles) for data used in this study. Ray paths of direct *P* waves are indicated by the grey curves, and *PP* bounce points are shown by open circles. Boxes denote the extent of a target volume at the depths of 0 and 2300 km. The location of point scatterers used in synthetic tests is indicated by solid circle.

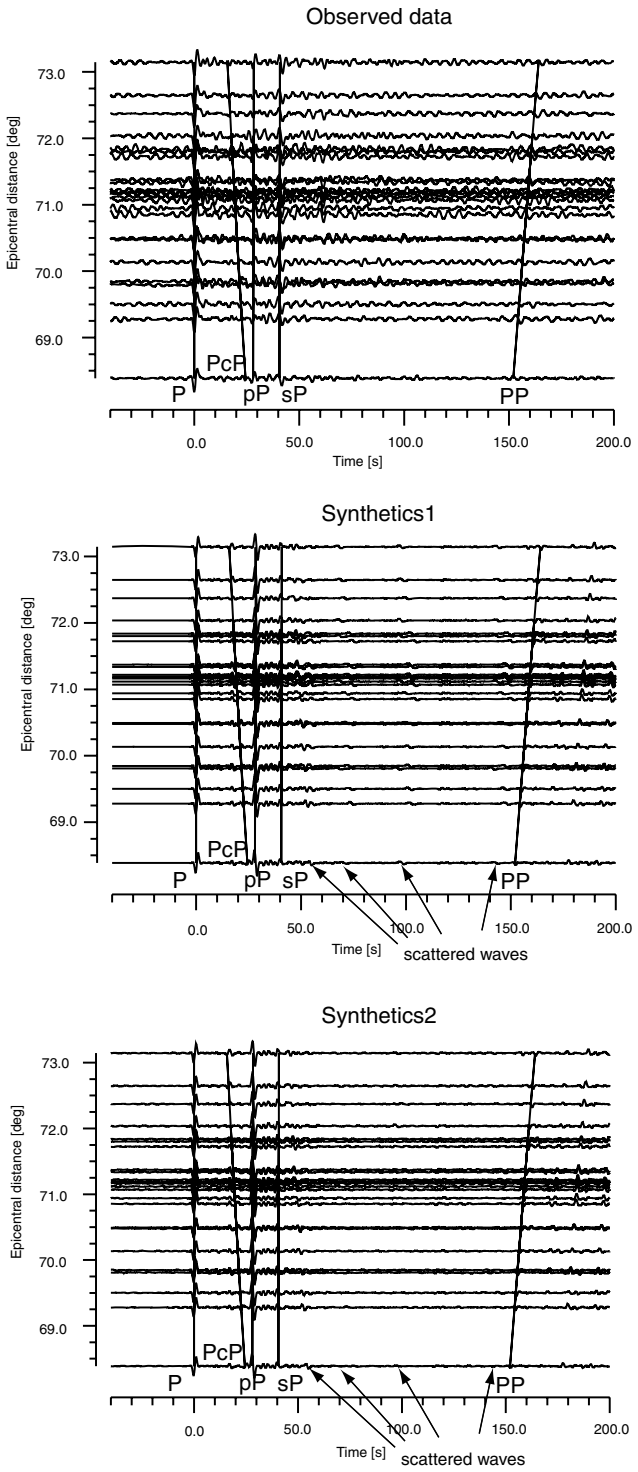

Figure 4. Examples of observed and synthetic seismograms used in this study. Data were recorded at the Californian seismic network from an intermediate-depth event in South America (latitude $= -19.78^\circ$, longitude $= -68.98^\circ$, and depth $= 133$ km). Scattered waves from five point scatterers at the depths of 0, 400, 800, 1200 and 1600 km are added to the synthetics. The amplitude of scattered waves is 20 per cent relative to *P* waves in synthetic 1 and 5 per cent in synthetic 2. In addition, real noise (the portion before *P* arrivals) is added to synthetic 2. The amplitude of noise is 5 per cent relative to *P* waves. Traces are aligned with respect to the direct *P* wave and are sorted by epicentral distances. A low pass filter with a corner frequency of 0.5 Hz is applied to both data and synthetics. Solid lines denote the theoretical traveltimes of *P*, *PcP*, *pP*, *sP* and *PP*.

first main wavelet of the direct *P* waves is 6 s, which is used as the length of the time window for stacking.

We generated synthetic seismograms using the reflectivity method (Müller 1985) and the IASP91 earth model (Kennett & Engdahl 1991), with the same source and receivers for the real data describe above. We placed five point scatterers at the gridpoints (latitude $= 10.4 \pm 0.3^\circ$ and longitude $= -70.5 \pm 0.4^\circ$) at the depths of 0, 400, 800, 1200 and 1600 km. The scattered waveforms simulated using a Gaussian function were added, and the same low-pass filter was to the synthetic waveforms. We prepared two versions of synthetic data (Fig. 4), one without noise and the other with noise. For the noise-free synthetics, the amplitude of the scattered waves was set to 20 per cent of the direct *P* wave, and for the synthetics with noise, it was set to 5 per cent of the direct *P* wave. Real noise was taken from the portion before the *P* arrival in the actual data described below, and the noise amplitude is set to the same level at the scattered waves (i.e. 5 per cent of the direct *P* wave). Each synthetic seismogram was then normalized by the maximum amplitude of the direct *P* wave. Since the amplitudes of standard phases such *P*, *PcP*, *pP* and *sP* are large compared to those of scattered waves, these standard phases were masked with the time window of 10 s.

The IASP91 standard earth model (Kennett & Engdahl 1991) was used to calculate the theoretical traveltimes of scattered waves as well as standard phases such as *P*, *PcP* and *PP*. The constant α was determined by synthetic tests. As mentioned earlier, there is a trade-off between reducing artefacts and retaining coherent scattered energy; if the constant value is too small, the weighting would be so strong that not only artefacts but also true signals are suppressed. The value of 0.16 was found to be optimal in this particular test.

4.2 Synthetic tests with point scatterers

Since the synthetics were generated assuming point scatterers, any migrated energy deviating from the scattering points is considered to be artefacts. With cross-correlation weighting, artefacts are reduced by ∼30–40 per cent in the horizontal direction (approximately parallel to ray path) and ∼40–50 per cent in the vertical direction, when compared to the result of conventional (non-weighted) migration (Figs 5a and b). The degree of artefact reduction is similar among the five point scatterers. The *PP* energy, underside reflection at Earth's surface, is better constrained with cross-correlation weighting than with the conventional migration. Because the bounce points of *PP* vary from station to station, the *PP* waveforms cannot be perfectly coherent at any single gridpoint, so their stacked energy is always reduced by the weighting. This is also true for the other standard phases such as *P*, *PcP*, depth phases and underside reflections at the mantle discontinuities, although these phases are masked in Fig. 5. The relatively large energy seen in the deeper portion with a conventional migration is attributed partly to *pPcP*, the depth phase of *PcP*, and partly to the crustal reverberation of the depth phase *pP*, both of which are not masked but effectively suppressed by the weighting.

The synthetics test with real noise and smaller scattered energy (5 per cent relative to *P* waves) provides a more realistic example (Figs 5c and d). The *PP* energy was removed in this example, and the overall energy level is smaller by an order of magnitude than the noise-free examples. Although the image quality somewhat deteriorates compared to the noise-free example, cross-correlation weighting still manages to highlight the scattering points, whereas it is difficult to identify them in conventional migration.

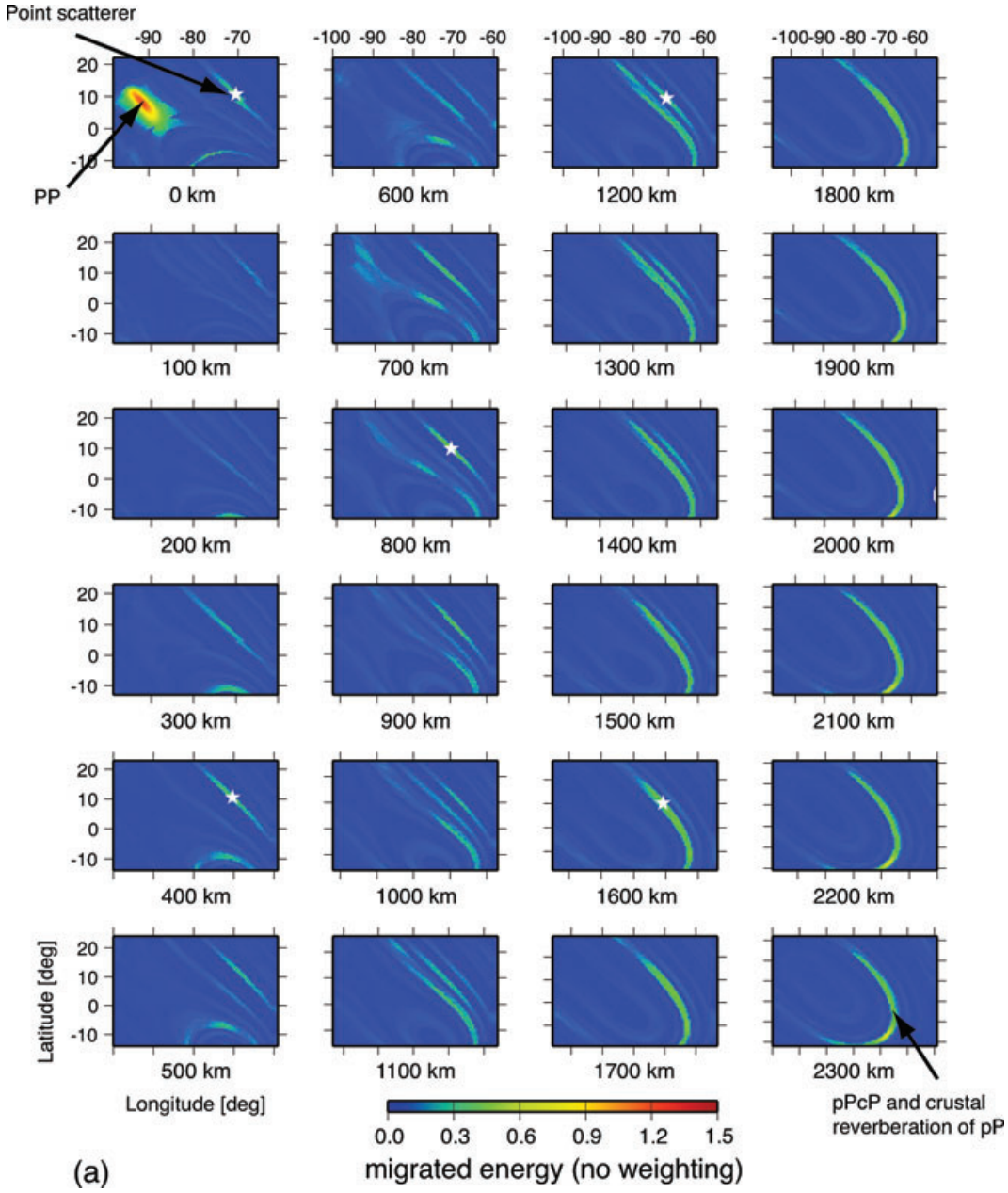

Figure 5. (a) Horizontal cross-sections of migrated energy, which is the square of stacked amplitude (eq. 1). *P*, *pP*, *sP* and *PcP* phases were masked. Locations of the point scatterers are indicated by the white stars. Conventional migration is applied to the synthetic data with 20 per cent scattering amplitude relative to *P*. (b) Same as (a) but with cross-correlation weighted migration. (c) Same as (a) but using the synthetics with 5 per cent scattering amplitude and 5 per cent real noise relative to *P*. Note that the colour scale is one-tenth of those in (a) and (b), and *PP* phase was removed. (d) Same as (c) but with cross-correlation weighted migration.

In the new scheme, migrated energy is controlled by the variance of time offsets, which is shown in Fig. 6. As expected, small variance is seen at the reflection points of *PP* at the surface and the scattering points. The variance corresponding to the *P* wave is also small, but this is simply because the phase is masked in this example. We also used unmasked synthetic seismograms that include all of the standard phases to see how the standard phases are constrained (Fig. 7). The energy levels of direct *P* wave and its depth phases, *pP* and *sP*, are much higher than those of the scattered waves. Because the depth phases are not coherent with respect to any gridpoint (see Fig. 8, point B), they are significantly suppressed by the weighting. Weaker but more coherent scattered waves (Fig. 8, point A) can still be recognized as in the test with masked synthetics.

4.3 Resolution test with closely located scatterers

Cross-correlation is calculated within a given time window, so if the time window happens to contain scattered waves from multiple gridpoints, the meaning of time offset determined by cross-correlation becomes ambiguous. When two scattered waves have significantly different amplitudes, for example, cross-correlation would be dominated by the larger one, so the weaker one, however coherent, is likely to be suppressed by weighting. If they have similar

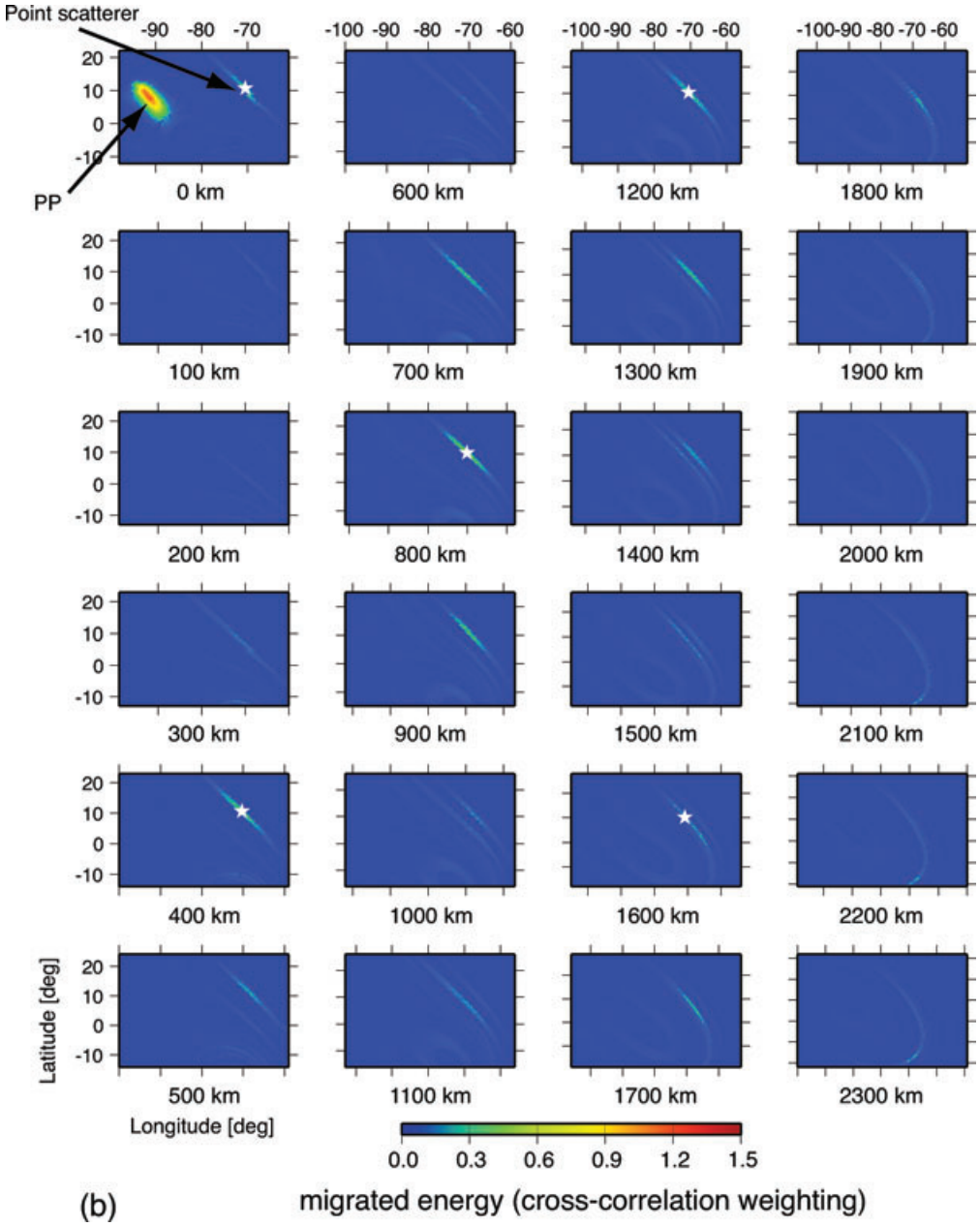

Figure 5. (*Continued.*)

amplitudes, on the other hand, both of them could be suppressed because cross-correlation may see them collectively as one incoherent scattered wave.

The above consideration implies a certain limitation to resolve closely located scatterers. Such limitation is expected to depend on the length of time window (or equivalently, the dominant frequency of scattered waves) and the gradient of theoretical traveltime in a target volume. The traveltime gradient is far from being uniform and also depends on source–receiver geometry. The resolving power of our migration scheme may thus vary from place to place in the mantle. A condition for resolving two scatterers may be expressed as $D\mathrm{d}t/\mathrm{d}s > \Delta t_{\mathrm{w}}$, where D is the distance between the scatterers, $\mathrm{d}t/\mathrm{d}s$ is the gradient of traveltime in the direction connecting them, and Δt_{w} is the length of time window.

As an example to demonstrate this issue, we conducted a synthetic test by using two identical point scatterers with different horizontal distances at the depth of 400 km (Fig. 9). In this case, resolution with our method is ∼150 km in the direction parallel to the ray path. No weighting results in slightly lower resolution (∼200 km). The resolution in the direction perpendicular to the ray path is much poorer even with the new scheme because of residual isochronal artefacts. In our source–receiver geometry, the distances of 100 and 200 km in the E–W direction correspond to the traveltime differences of ∼6.5 and ∼12.5 s, respectively, at the depth of 400 km. Because the length of the time window here is 6 s, the resolution of 150 km is consistent with what is expected from the above order-of-magnitude argument.

4.4 Sensitivity to noise

We also performed synthetic tests to further examine the stability of migration with respect to noise. In the tests with noise shown in

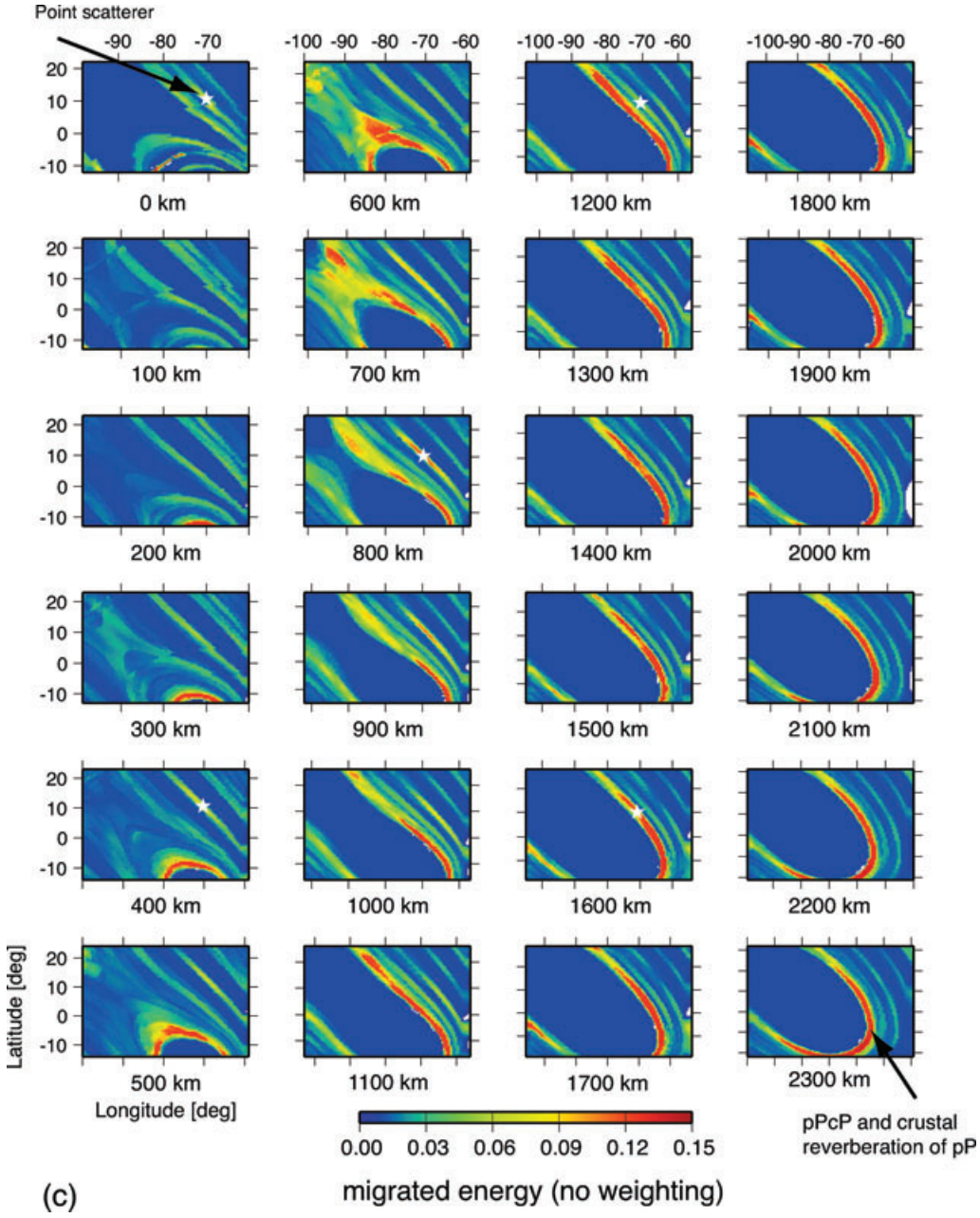

Figure 5. (*Continued.*)

Figs 5(c) and (d), the amplitude of noise is at the same level for that of scattered wave (5 per cent of direct *P*), and here we vary the noise amplitude up to 10 per cent of direct *P* while keeping the amplitude of scattered wave (Fig. 10). As described in the Section 3.3, the amplitude of the scattered wave would be significantly reduced if only cross-correlation weighting (i.e. without semblance information) is applied to noisy data. With the hybrid weighting of eq. (8), the contribution of weighting determined by cross-correlation becomes smaller and that of semblance becomes larger as noise level increases. This makes it possible to retain scattered energy with minimum reduction and to suppress the noise efficiently even at the higher noise levels, so the scattered energy can be identified with confidence. Because most of real seismograms are contaminated by signal-generated noise, this stability makes the new migration scheme a practical application.

5 DISCUSSION

5.1 Comparison between SBWM and CCWM

Using the real broadband data described in the section of 4.1, we compared conventional (no weighting) migration (e.g. Freybourger *et al.* 2001; Kito *et al.* 2003; Thomas *et al.* 2004), slowness-backazimuth weighted migration (SBWM) (Kito *et al.* 2007), and cross-correlation weighted migration (CCWM). No significant scattered waves are recognized in this particular data set, so masking was not applied to the data in order to focus on how the standard phases are imaged with these different methods. The energy at the surface (0 km depth) corresponds to the *PP* bounce points on the western side of Costa Rica, and the large energy in the lower mantle is owning to the direct *P* waves whose turning points are approximately at

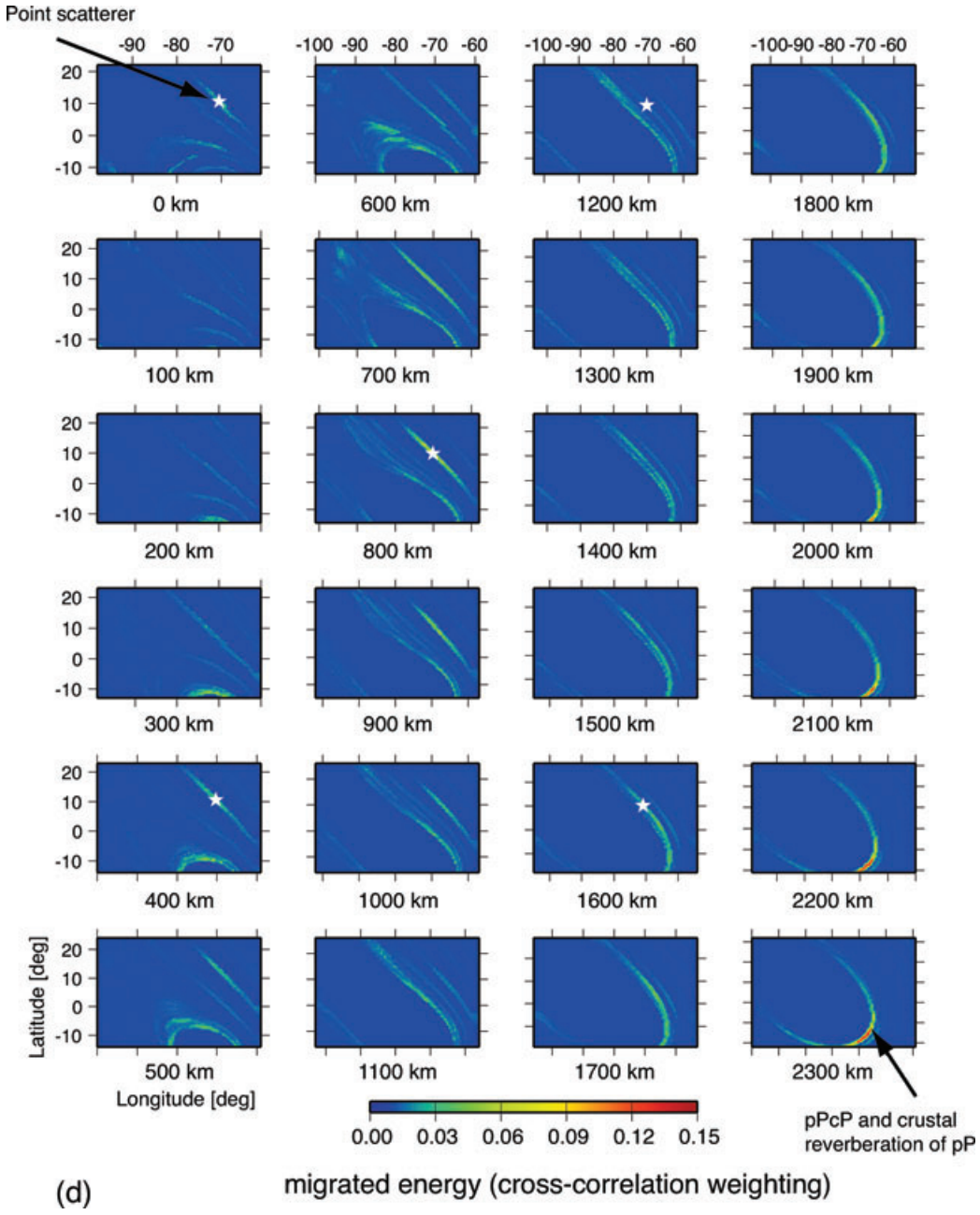

Figure 5. (*Continued.*)

1950 km depth. The weaker energy surrounding the direct *P* waves is caused by their depth phases, *pP* and *sP*. The ray paths of these depth phases are very different from those of any scattered waves from the gridpoints considered here, so the majority of artefacts caused by depth phases are suppressed by weighting both in SBWM and in CCWM (Fig. 11). The fundamental difference between them is that SBWM assumes plane waves for weighting in which slowness is constant throughout all stations whereas CCWM directly takes account of the slowness change of scattered waves from station to station through measuring time offsets at each station. This difference may be seen in how the depth phases are suppressed. While the depth phases are spatially better constrained in SBWM, their maximum energy (at the depth of ∼1600 km) is smaller (i.e. more efficiently reduced) in CCWM. We also see that standard phases such as *PP* and *P*, which have smaller changes in slowness than scattered waves, are imaged more properly with SBWM than with CCWM, and the focusing of these standard phases is actually better with SBWM. In other words, CCWM is more suitable to detect scattered waves than SBWM. Note that SBWM has two free parameters related to slowness and backazimuth whereas CCWM has only one (α in eq. 5), so it is easier for CCWM to arrive at an optimal value by exploring the parameter space.

The *PP* energy is better constrained with SBWM and CCWM than with non-weighted migration. The degree of *PP* energy reduction, however, is slightly different between SBWM and CCWM, because of complex *PP* waveforms likely caused by sediment layers at the ocean bottom in the vicinity of the *PP* reflection points. Weighting in CCWM is based partly on the coherency of each

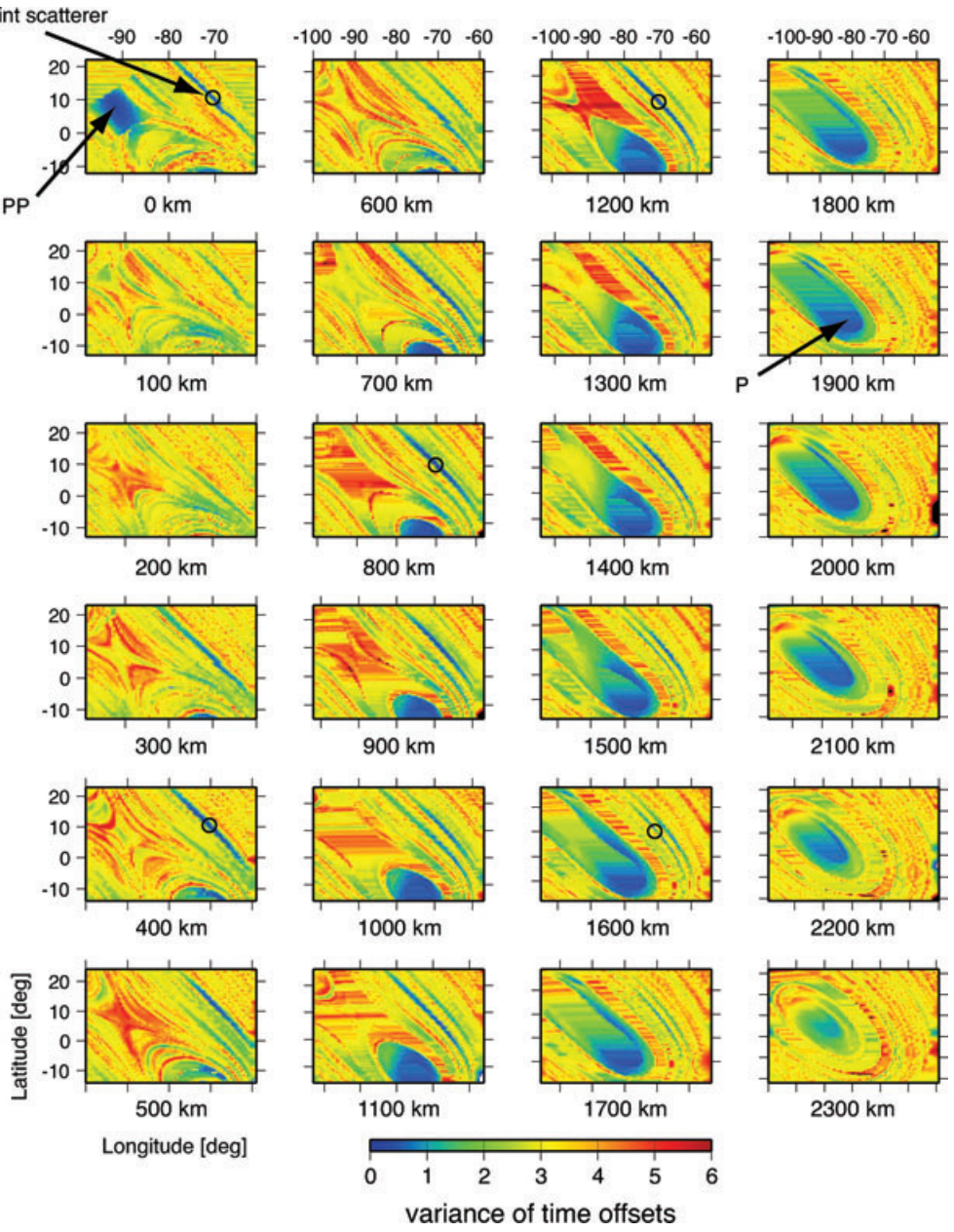

Figure 6. Variance of time offsets (σ_t^2) corresponding to Fig. 5(b). Point scatterers are denoted by open circles.

waveform pair at each gridpoint whereas that in SBWM takes into account, in effect, the overall waveform coherency through stacking with respect to other neighbouring gridpoints. In other words, SBWM is based on relative waveform coherency, thus being less sensitive to waveform distortion.

5.2 Note on development history

For any migration gridpoint, one can define a quasi-isochronal volume, which contains other gridpoints with similar sets of source–receiver traveltimes. The true scattering point is expected to have the maximum migrated energy within the volume, so theoretically speaking, we can implement a weighted migration scheme just by searching (i.e. without calculating cross-correlation); for each gridpoint, we search for maximum migrated energy within its quasi-isochronal volume and then use a distance to the gridpoint with maximum energy for weighting (as in SBWM). We initially tried to implement this idea but found it impractical as explained below.

In this search-based algorithm, we first need to define a quasi-isochronal volume for each gridpoint, using some threshold on traveltime difference. Because every gridpoint has N_r theoretical traveltimes and thus N_r traveltime differences with respect to a reference (true) gridpoint, we may impose a criterion on their rms average. It turned out that the number of grids contained in a quasi-isochronal volume varies considerably from grid to grid, from a few to several thousands (e.g. Fig. 2), reflecting variations in traveltime gradient within the mantle. A smaller gradient results in a larger quasi-isochronal volume. Although this approach does not require any further stacking (as in SBWM) or coherency measurement (as in CCWM), it does demand a large amount of computational

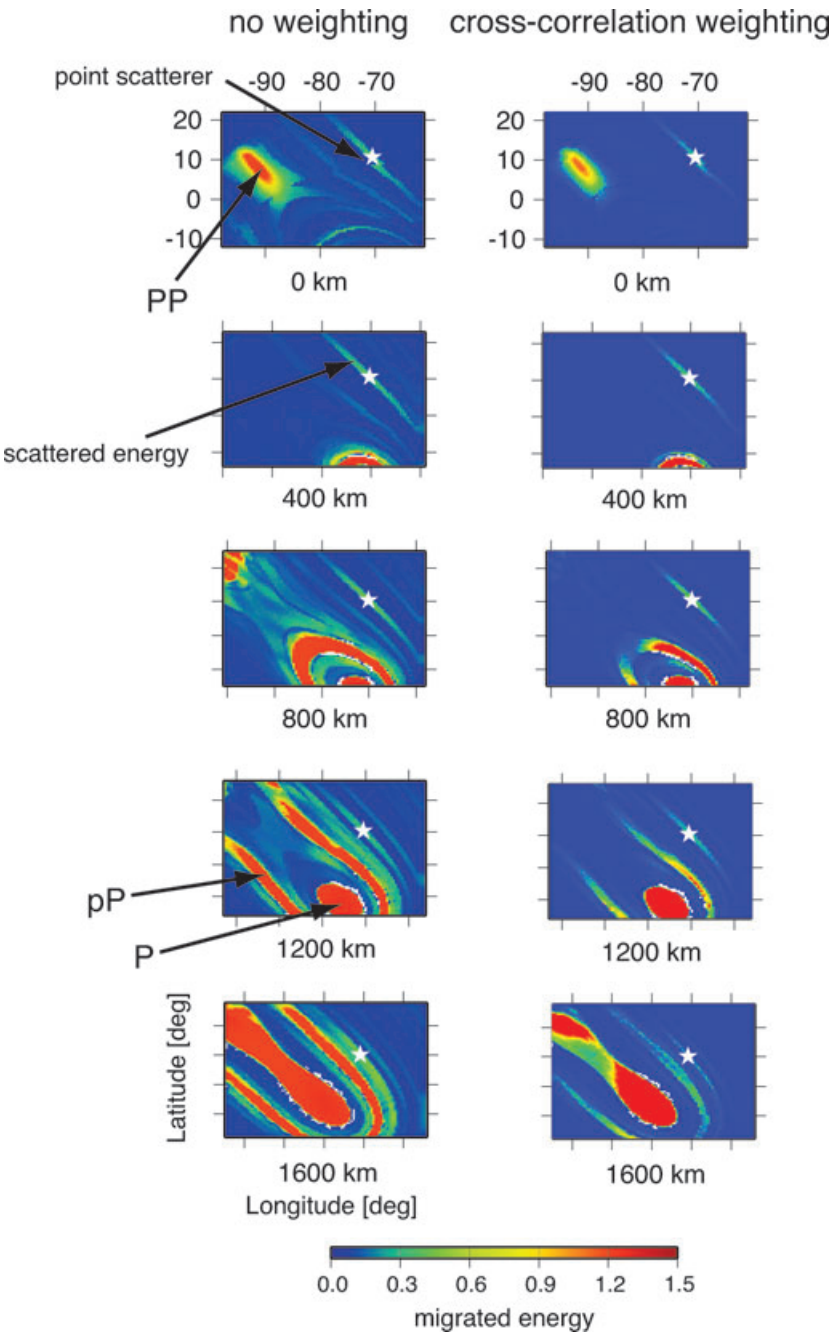

Figure 7. Migration results using the synthetic data without masking standard phases. Horizontal cross-sections are shown at five depths. Left- and right-hand panels correspond to, respectively, conventional migration and cross-correlation weighted migration. Stars denote the locations of point scatterers. Depth phases, strong but incoherent signals, are reduced by cross-correlation weighting, making it easier to identify weaker but coherent scattered energy. The energy of *P* and *pP* is so high that they are saturated in the colour scale adopted here.

memory to store all quasi-isochronal volumes, which also makes subsequent search time-consuming. The simplicity of the algorithm is appealing, and this approach may eventually become competitive with the progress of computational resources, but it appears that the cross-correlation scheme is more practical at present.

5.3 Numerical efficiency

A critical difference between SBWM and CCWM is their numerical efficiency, because there is no major difference between them in terms of the quality of migrated image, as discussed in 5.1. If the number of sampling points in the time window is denoted by L, the number of floating point operations for linear stacking is proportional to the number of gridpoints N_g, the number of receivers N_r, and the number of sampling points L, so in total it requires $O(N_g N_r L)$ operations. This operation is common to both methods. In SBWM, stacking is repeated for a range of slowness-backazimuth pairs at every gridpoint to find the maximum energy, and the number of necessary operations is proportional to the number of slowness-backazimuth combinations N_{sb}, the number of gridpoints N_g, the

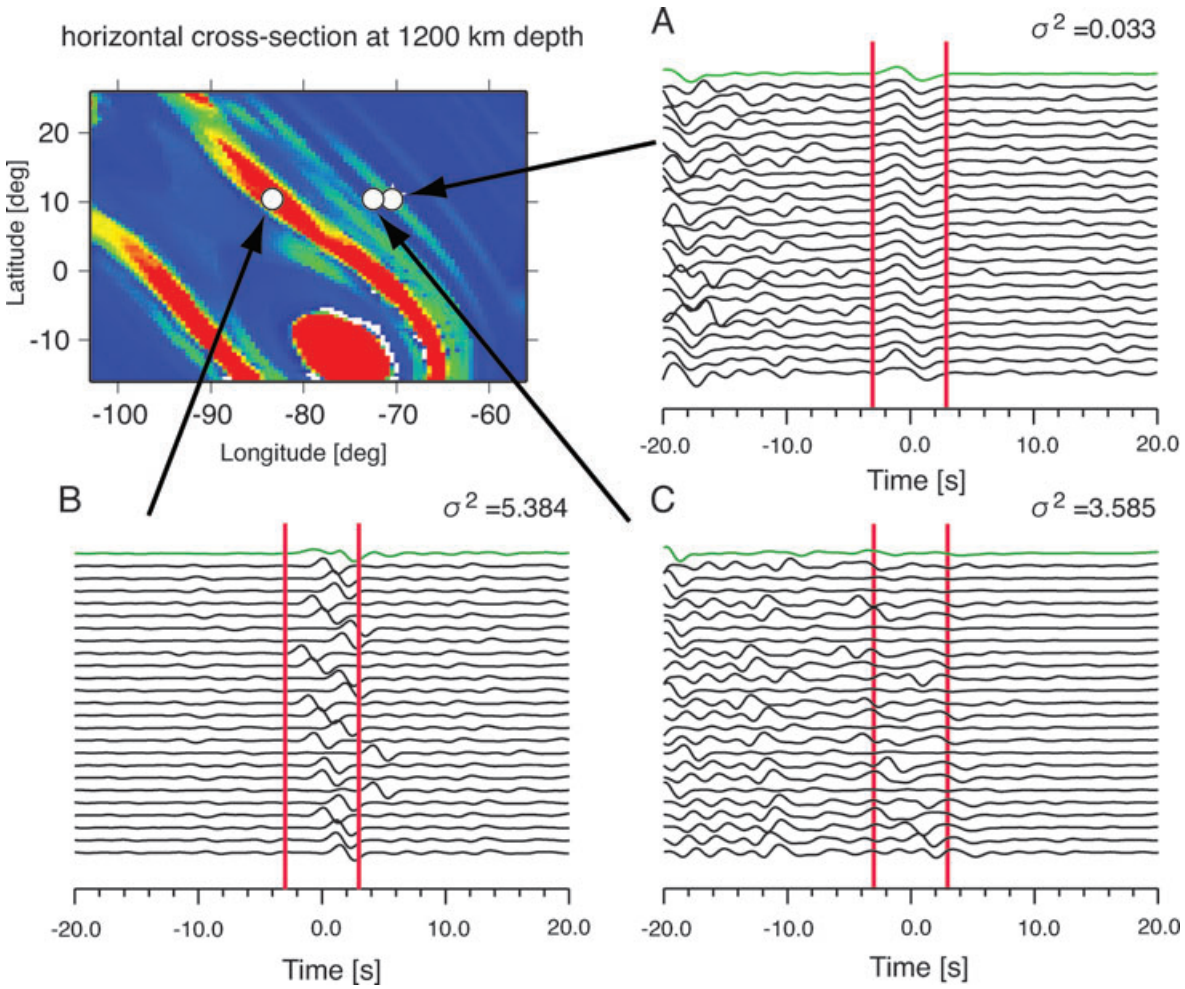

Figure 8. Horizontal cross-section at the depth of 1200 km showing migrated energy by conventional migration using synthetics without masking (upper left-hand panel). (A) Pre-stack seismograms shifted with respect to the true scattering point. (B) Same as (A) but shifted with respect to one of gridpoints where strong but incoherent depth phase is observed. (C) Same as (A) but shifted with respect to one of gridpoints slightly off the true scattering point. σ^2 is the variance of time offsets. Red lines denote the time window used for stacking. Top green traces are stacked waveforms using all traces.

number of receivers N_r, and the number of sampling points in a stacking window. The time window used for stacking process in the slowness-backazimuth field is typically twice as long as that for stacking in conventional migration (Kito *et al.* 2007). Thus, the number of required operations is $O(2N_gN_rN_{sb}L)$. On the other hand, most of floating point operations in CCWM are used to calculate cross-correlation and semblance, so the number of operations in CCWM is $O[N_gN_r(L^2 + 2L)]$ if cross-correlation is evaluated in the time domain and $O[N_gN_r(L \log_2 L + 2L)]$ in the Fourier domain; the latter is a natural choice for implementation. Since the calculation of semblance needs two stacks over time window and stations, $O(2N_gN_rL)$ in both cases (i.e. in the time and Fourier domains) represents semblance calculation, and the rest corresponds to cross-correlation.

An improvement in efficiency may thus be quantified as the ratio between the number of operations used for weighting in SBWM and in CCWM, $O[2N_{sb}/(\log_2 L + 2)]$. Because N_{sb} is typically $\sim 10^3$ and L is $\sim 10^2$, CCWM is expected to be faster than SBWM by about two orders of magnitude. This drastic increase in computational speed would be best appreciated when building a robust migration image with modern statistical techniques such as bootstrap resampling.

5.4 Applications to real Earth structures

Our coherency-based signal enhancement could potentially be jeopardized by various realistic complications, though many of them can be resolved in a relatively straightforward manner. Waveform misalignment due to 3-D heterogeneities absent from the assumed background velocity model, for example, can be minimized by incorporating 3-D velocity structure when preparing source–receiver traveltimes for all gridpoints. 3-D ray tracing is more time-consuming, but it has to be done only once prior to migration, so this additional care does not affect the efficiency of CCWM itself. Corrections for geometrical spreading are also easy to accommodate as done in Kirchhoff migration. The presence of background noise as well as signal-generated noise is certainly a concern if their amplitudes are large, and our strategy is to combine cross-correlation and semblance in order to stabilize the coherency measurement as much as possible. It is noted that any migration method would fail to image weak scatterers if the signal-to-noise ratio is too low.

Our primary goal has been to develop an efficient migration method to better locate small-scale scatterers and resolve their shapes, and it should be noted that weighted images are not readily interpretable as specific medium perturbations. Such physical

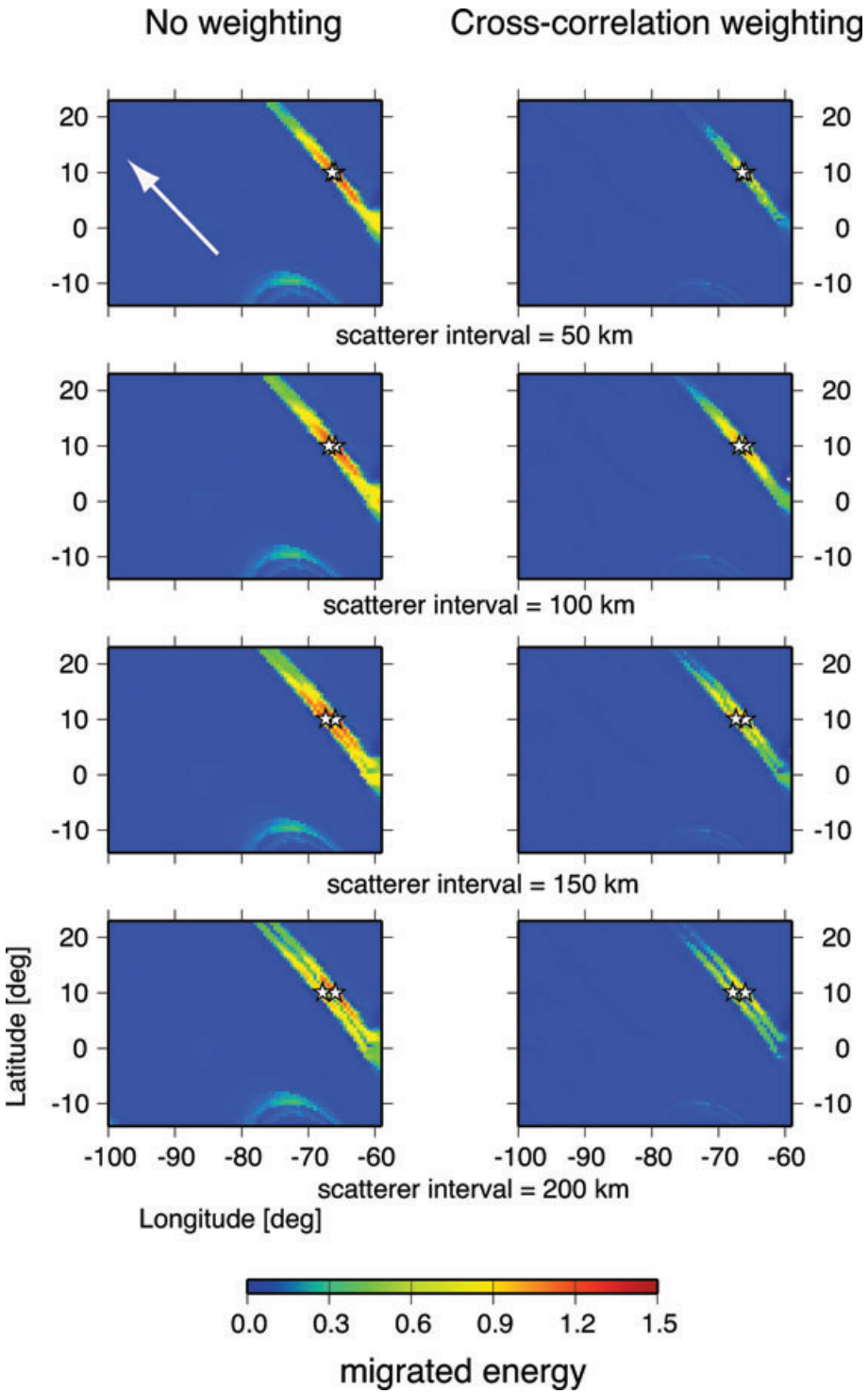

Figure 9. Migration image for two closely located scatterers (denoted by stars) placed at the depth of 400 km. The white arrow indicates the direction of ray path of direct *P*. Left- and right-hand panels show results by conventional migration and cross-correlation weighted migration, respectively. Distance between the scatterers is varied from 50 to 200 km.

interpretations may be done most accurately by, for example, comparing observed waveforms to synthetic seismograms calculated with a realistic background earth model, once we have identified target scatterers to be simulated.

Based on various chemical mixing models in mantle dynamics, we expect that there is a statistical distribution of small-scale heterogeneities in the mantle. What is also expected in the continual re-mixing of chemical heterogeneities is a size-number distribution (i.e. the number of blobs increases as their size decreases) because destroying a large blob by mixing would create numerous smaller blobs. Although it is impossible to image the entire spectrum of these heterogeneities given the limited seismic resolution (Section 4.3), we can potentially image the upper end of such spectrum by migration in a deterministic manner.

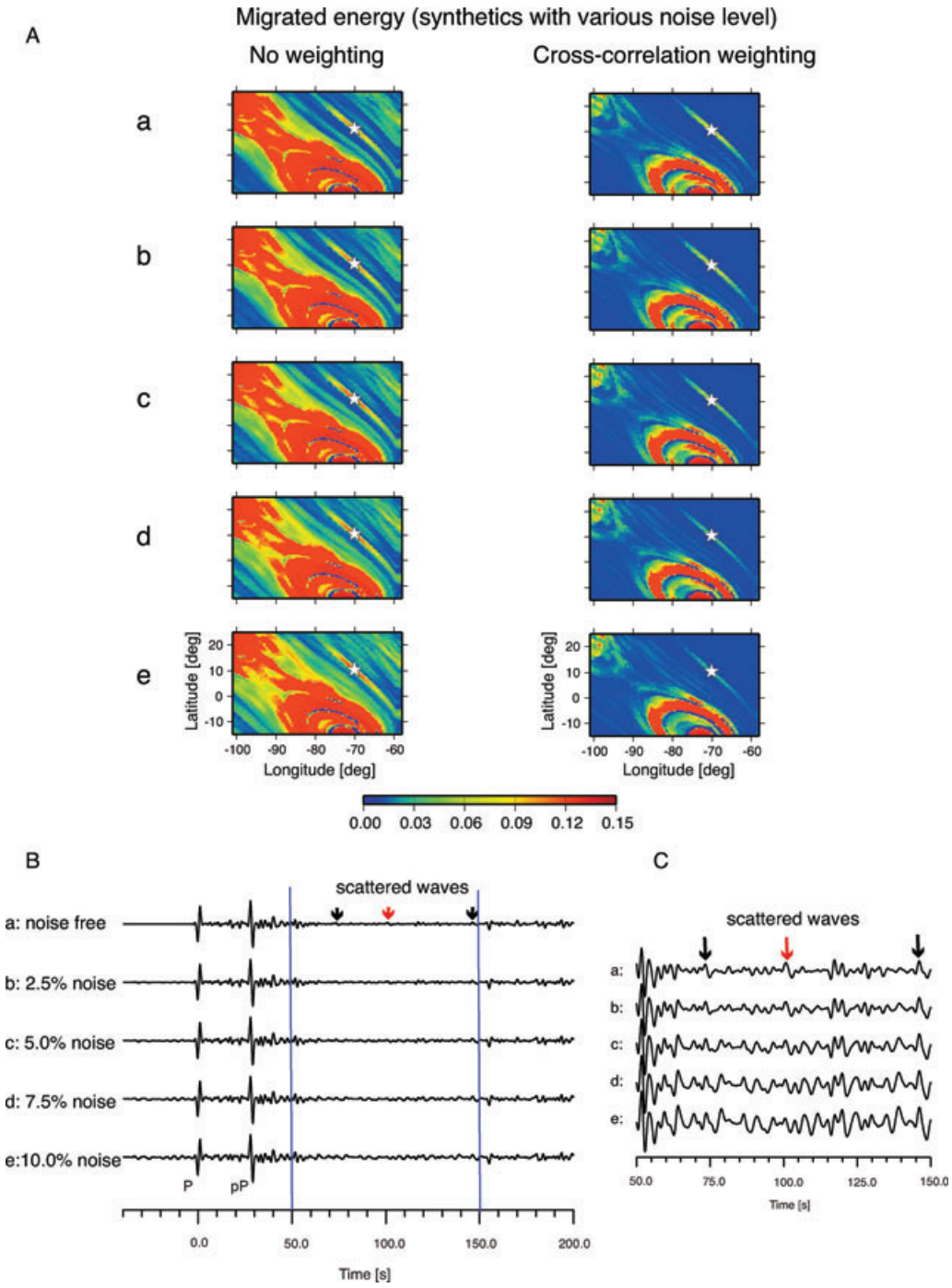

Figure 10. (A) Effects of noise on migration results. A horizontal cross-section at the depth of 800 km is shown for the case of conventional migration (left-hand panel) and cross-correlation weighted migration (right-hand panel) with varying noise levels: (a) 0 per cent, (b) 2.5 per cent, (c) 5 per cent, (d) 7.5 per cent and (e) 10 per cent. The amplitude of noise is measured with respect to that of *P* wave. (B) Synthetic seismograms are shown for each noise level. (C) A magnified view of scattered waves within the time window of 50–150 s (denoted by vertical bars in B). Note that the amplitudes of scattered wave and noise are approximately the same in (c).

ACKNOWLEDGMENTS

This work was sponsored by the U.S. National Science Foundation under grant EAR-0842753. Figures were generated with GMT (Wessel & Smith 1995), and Seismic Handler (Stammler 1993) was used for data analysis. Data used in this study were obtained from the IRIS Data Management Center. We thank Editor Mike Kendall and two anonymous reviewers for constructive comments and suggestions.

REFERENCES

Allègre, C.J. & Turcotte, D.L., 1986. Implications of a 2-component marble-cake mantle, *Nature,* **323,** 123–127.

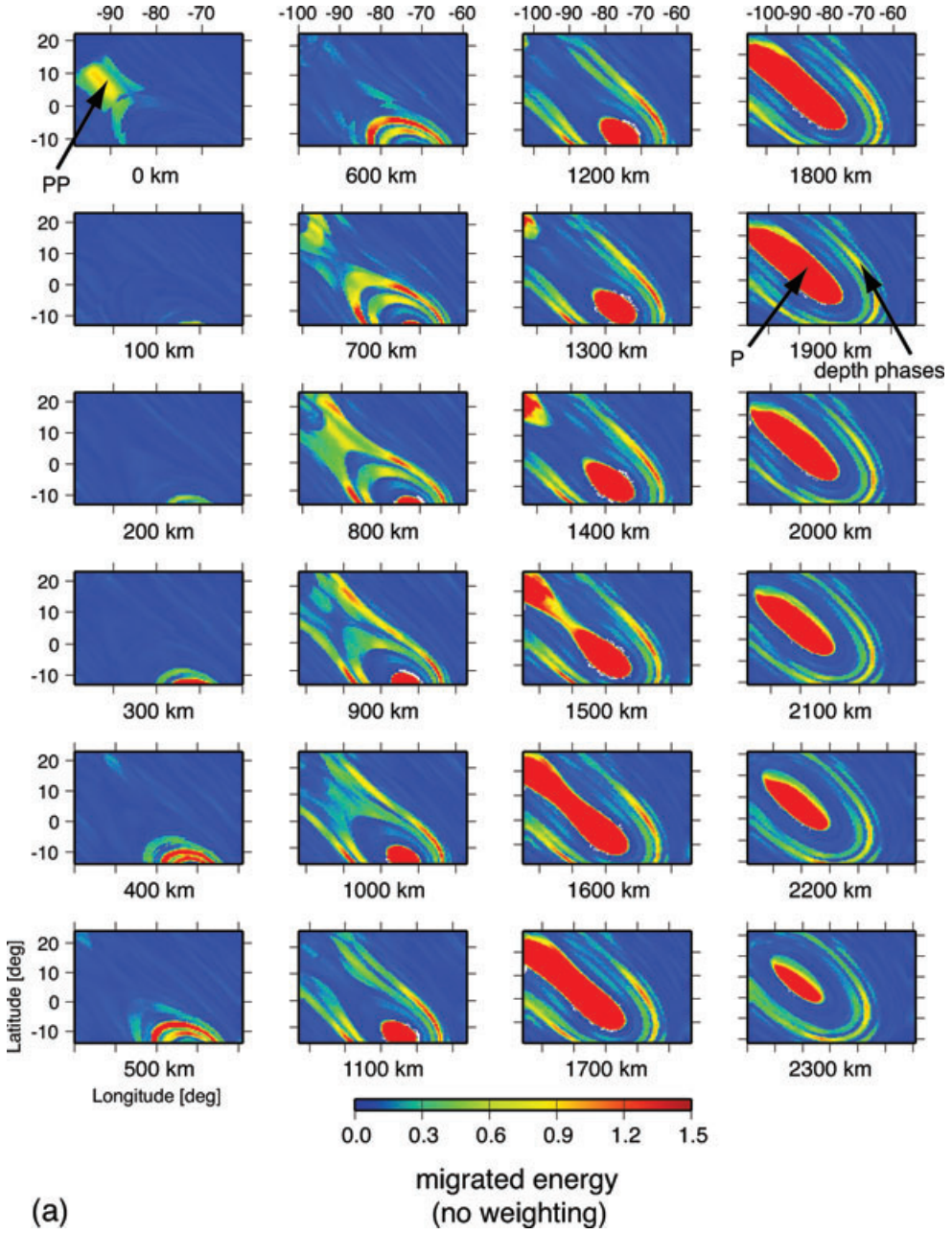

Figure 11. (a) Migration image with real data, produced by conventional migration. No masking was applied. Note that the energy of direct *P* is so high that it is saturated in the colour scale adopted here. (b) Same as (a) but with slowness backazimuth weighted migration (Kito *et al.* 2007). (c) Same as (a) but with cross-correlation weighted migration.

Bilek, S.L. & Lay, T., 1998. Lower mantle heterogeneity beneath Eurasia imaged by parametric migration of shear waves, *Phys. Earth planet. Int.,* **108,** 201–208.

Chambers, K. & Woodhouse, J.H., 2006. Investigating the lowermost mantle using migration of long-period S-ScS data, *Geophys. J. Int.,* **166,** 667–678.

Christensen, U.R. & Hofmann, A.W., 1994. Segregation of subducted oceanic crust in the convecting mantle, *J. geophys. Res.,* **99,** 19867–19884.

Cordery, M.J., Davies, G.F. & Campbell, I.H., 1997. Genesis of flood basalts from eclogite-bearing mantle plumes, *J. geophys. Res.,* **102,** 20 179–20 197.

Freybourger, M., Chevrot, S., Krüger, F. & Achauer, U., 2001. A waveform migration for the investigation of P wave structure at the top of D''beneath northern Siberia, *J. geophys. Res.,* **106,** 4129–4140.

Fukao, Y., Widiyantoro, S. & Obayashi, M., 2001. Stagnant slabs in the upper and lower mantle transition region, *Rev. Geophys.,* **39,** 291–323.

Hedlin, M.A. H., Shearer, P.M. & Earle, P.S., 1997. Seismic evidence for small-scale heterogeneity throughout the Earth's mantle, *Nature,* **387,** 145–150.

Helffrich, G.R. & Wood, B.J., 2001. The Earth's mantle, *Nature,* **412,** 501–507.

Hofmann, A.W., 1997. Mantle geochemistry: the message from oceanic volcanism, *Nature,* **385,** 219–229.

Hutko, A., Lay, T., Revenaugh, J. & Garnero, E.J., 2008. Anticorrelated seismic velocity anomalies from post-perovskite in the lowermost mantle, *Science,* **320,** 1070–1074.

Hutko, A.R., Lay, T., Garnero, E.J. & Revenaugh, J., 2006. Seismic detection of folded, subducted lithosphere at the core-mantle boundary, *Nature,* **441,** 333–336.

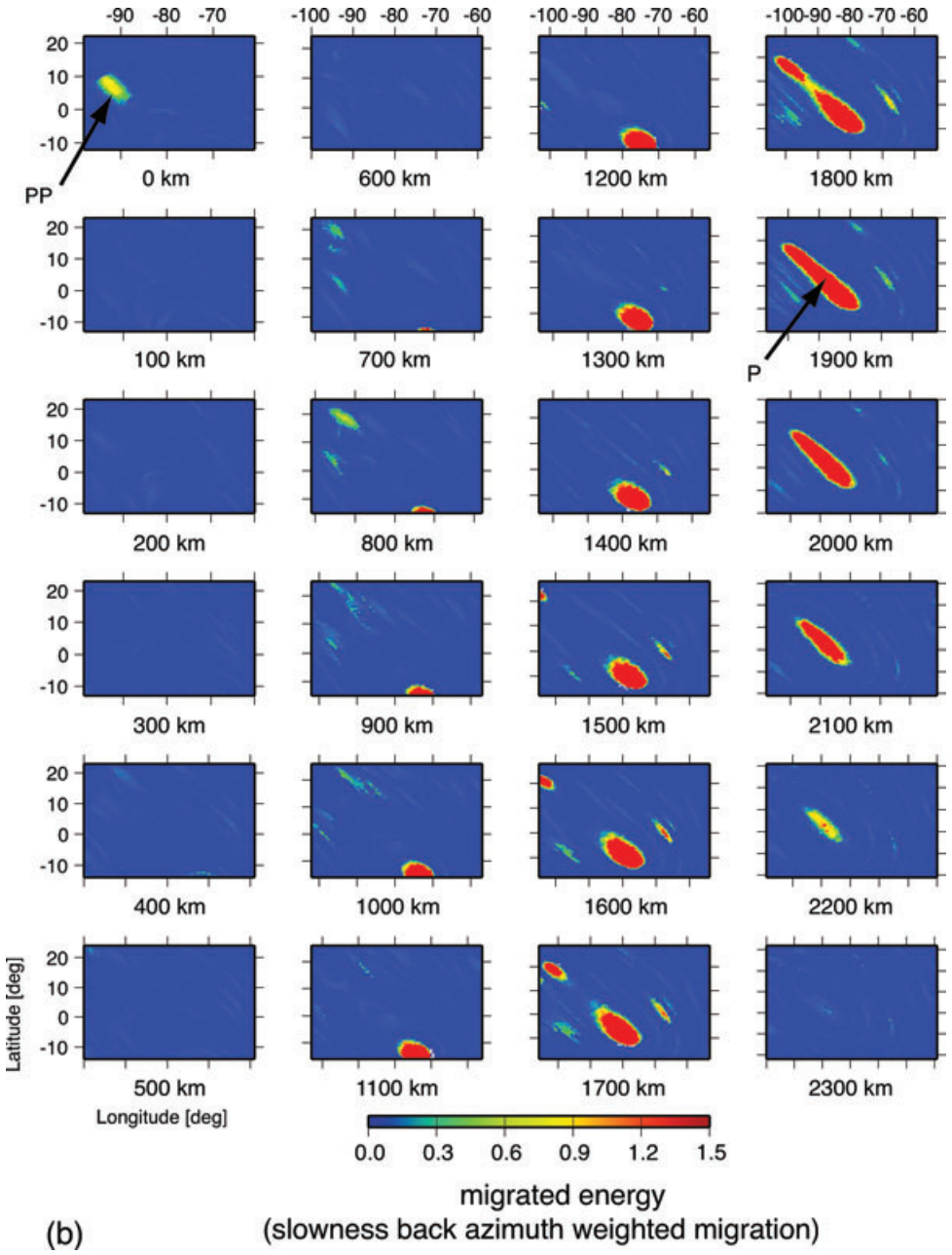

Figure 11. (*Continued.*)

Ito, G. & Mahoney, J.J., 2005. Flow and melting of a heterogeneous mantle: 2. Implications for a chemically nonlayered mantle, *Earth planet. Sci. Lett.,* **230,** 47–63.

Kaneshima, S., 2003. Small-scale heterogeneity at the top of the lower mantle around the Mariana slab, *Earth planet. Sci. Lett.,* **209,** 85–101.

Kaneshima, S. & Helffrich, G., 1999. Dipping low-velocity layer in the mid-lower mantle: evidence for geochemical heterogeneity, *Science,* **283,** 1888–1891.

Karason, H. & van der Hilst R.D., 2001. Tomographic imaging of the lowermost mantle with differential times of refracted and diffracted core phases (PKP, Pdiff), *J. geophys. Res.,* **106,** 6569–6587.

Karato, S., 1997. On the separation of crustal component from subducted oceanic lithosphere near the 660 km discontinuity, *Phys. Earth planet. Int.,* **99,** 103–111.

Kellogg, L.H., Hager, B.H. & van der Hilst, R.D., 1999. Compositional stratification in the deep mantle, *Science,* **283,** 1881–1884.

Kennett, B.L.N. & Engdahl, E.R., 1991. Traveltimes for global earthquake location and phase identification, *Geophys. J. Int.,* **105,** 429–465.

Kennett, B.L.N., Widiyantoro, S. & van der Hilst, R.D., 1998. Joint seismic tomography for bulk-sound and shear wavespeed in the Earth's mantle, *J. geophys. Res.,* **103,** 12 469–12 593.

Kito, T. & Krüger, F., 2001. Heterogeneities in D'' beneath the southwestern Pacific inferred from scattered and reflected P waves, *Geophys. Res. Lett.,* **28,** 2545–2548.

Kito, T., Shibutani, T. & Hirahara, K., 2003. Scattering objects in the lower mantle beneath northeastern China observed with a short-period seismic array, *Phys. Earth planet. Int.,* **138,** 55–69.

Kito, T., Rietbrock, A. & Thomas, C., 2007. Slowness backazimuth weighted migration: a new array approach to a high-resolution image, *Geophys. J. Int.,* **169,** 1201–1209.

Kito, T., Thomas, C., Rietbrock, A., Garnero, E.J., Nippress, S. & Heath, A.E., 2008. Seismic evidence for a sharp lithospheric base persisting

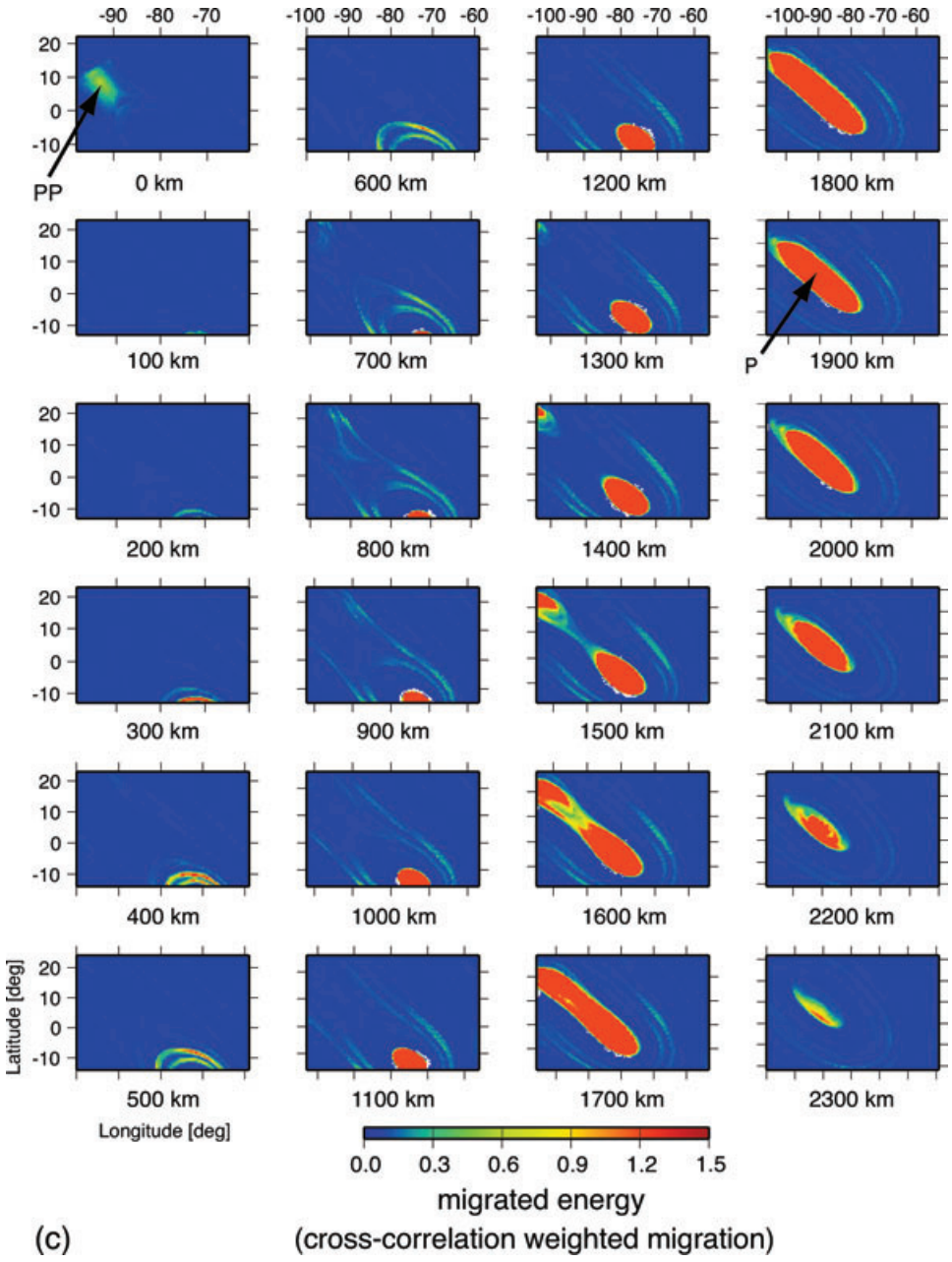

Figure 11. (*Continued.*)

to the lowermost mantle beneath the Caribbean, *Geophys. J. Int.,* **174,** 1019–1028.

Korenaga, J., 2004. Mantle mixing and continental breakup magmatism, *Earth planet. Sci. Lett.,* **218,** 463–473.

Korenaga, J., 2005. Why did not the Ontong Java Plateau form subaerially?, *Earth planet. Sci. Lett.,* **234,** 385–399.

Korenaga, J., 2006. Archean geodynamics and the thermal evolution of Earth, in *Archean Geodynamics and Environments,* pp. 7–32, eds Benn, K., Mareschal, J.-C. & Condie, K., American Geophysical Union, Washington, DC.

Korenaga, J., 2008a. Urey ratio and the structure and evolution of Earth's mantle, *Rev. Geophys.,* **46,** RG2007, doi:10.1029/2007RG000241.

Korenaga, J., 2008b. Plate tectonics, flood basalts, and the evolution of Earth's oceans, *Terra Nova,* **20,** 419–439.

Korenaga, J. & Kelemen, P.B., 2000. Major element heterogeneity of the mantle source in the North Atlantic igneous province, *Earth planet. Sci. Lett.,* **184,** 251–268.

Krüger, F., Scherbaum, F., Weber, M. & Schlittenhardt, J., 1996. Analysis of asymmetric multipathing with a generalization of the double-beam method, *Bull. seis. Soc. Am.,* **86,** 737–749.

Lay, T. & Young, C.J., 1996. Imaging scattering structures in the lower mantle by migration of long period S waves, *J. geophys. Res.,* **101,** 20 023–20 040.

Lee, C.-T.A. & Chen, W.P., 2007. Possible density segregation of subducted oceanic lithosphere along a weak serpentinite layer and implications for compositional stratification of the earth's mantle, *Earth planet. Sci. Lett.,* **255,** 357–366.

Lyubetskaya, T. & Korenaga, J., 2007. Chemical composition of Earth's primitive mantle and its variance, 2, implications for global geodynamics, *J. geophys. Res.,* **112,** B03212, doi:10.1029/2005JB004224.

Manga, M., 1996. Mixing of heterogeneities in the mantle: effect of viscosity differences, *Geophys. Res. Lett.,* **23,** 403–406.

Margerin, L. & Nolet, G., 2003. Multiple scattering of high-frequency seismic waves in the deep Earth: PKP precursor analysis and

inversion for mantle granularity, *J. geophys. Res.,* **108,** 2514, doi:10.1029/2003JB002455.

Müller, G., 1985. The reflectivity method: a tutorial, *J. Geophys.,* **58,** 153–174.

Neidell, N.S. & Taner, M.T., 1971. Semblance and other coherency measures for multichannel data, *Geophysics,* **36,** 482–497.

Revenaugh, J., 1995. A scattered-wave image of subduction beneath the transverse ranges, *Science,* **268,** 1888–1892.

Ringwood, A.E. & Irifune, T., 1988. Nature of the 650-km seismic discontinuity—implications for mantle dynamics and differentiation, *Nature,* **331,** 131–136.

Rost, S., Garnero, E.J. & Williams, Q., 2008. Seismic array detection of subducted oceanic crust in the lower mantle, *J. geophys. Res.,* **113,** B06303, doi:10.1029/2007JB005263.

Scherbam, F., Krüger, F. & Weber, M., 1997. Double beam imaging: mapping lower mantle heterogeneities using combinations of source and receiver arrays, *J. geophys. Res.,* **102,** 507–522.

Schimmel, M. & Paulssen, H., 1997. Noise reduction and detection of weak, coherent signals through phase-weighted stacks, *Geophys. J. Int.,* **130,** 487–505.

Sleep, N.H., 1984. Tapping of magmas from ubiquitous mantle heterogeneities: an alternative to mantle plumes? *J. geophys. Res.,* **89,** 10 029–10 041.

Stammler, K., 1993. Seismic handler—programmable multichannel data handler for interactive and automatic processing of seismological analysis, *Comp. Geosci.,* **19,** 135–140.

Thomas, C., Kendall, J.-M. & Lowmann, J., 2004. Lower mantle seismic discontinuities and the thermal morphology of subducted slabs, *Earth planet. Sci. Lett.,* **225,** 105–113.

Trampert, J., Deschamps, F., Resovsky, J. & Yuen, D., 2004. Probabilistic tomography maps chemical heterogeneities throughout the lower mantle, *Science,* **306,** 853–856.

van der Hilst, R.D., Widiyantoro, S. & Engdahl, E.R., 1997. Evidence for deep mantle circulation from global tomography, *Nature,* **386,** 578–584.

van Keken, P.E., Karato, S. & Yuen, D.A., 1996. Rheological control of oceanic crust separation in the transition zone, *Geophys. Res. Lett.,* **23,** 1821–1824.

van Keken, P.E., Hauri, E.H. & Ballentine, C.J., 2002. Mantle mixing: the generation, preservation, and destruction of chemical heterogeneity, *Annu. Rev. Earth planet. Sci.,* **30,** 493–525.

Vanacore, E., Niu, F. & Kawakatsu, H., 2006. Observations of the mid-mantle discontinuity beneath indonesia from S to P converted waveforms, *Geophys. Res. Lett.,* **33,** L04302, doi:10.1029/2005GL025106.

Wessel, P. & Smith, W.H.F., 1995. New version of the generic mapping tools released, *EOS, Trans. Am. geophys. Un.,* **76,** 329.

Zindler, A. & Hart, S., 1986. Chemical geodynamics, *Annu. Rev. Earth planet. Sci.,* **14,** 493–571.